Analyzing the Grell-Freitas convection scheme from hydrostatic to nonhydrostatic scales within a global model

Laura D. Fowler[1], William C. Skamarock[1], Georg A. Grell[2],
Saulo R. Freitas[3], and Michael G. Duda[1]

[1]National Center for Atmospheric Research*, Boulder, Colorado, USA.

[2]Earth Systems Research Laboratory of the National Oceanic and Atmospheric Administration (NOAA), Boulder, Colorado, USA.

[3]Center for Weather Forecasting and Climate Studies, INPE, Cachoeira, Sao Paulo, Brazil.

Revised for Monthly Weather Review
February 27th 2016

---

* The National Center for Atmospheric Research is sponsored by the National Science Foundation.

Corresponding author address: Dr. Laura D. Fowler, National Center for Atmospheric Research, P.O. Box 3000, Boulder, CO, 80307-3000. E-mail: laura@ucar.edu.

ABSTRACT

We implemented the Grell and Freitas (GF) parameterization of convection in which the cloud base mass flux varies quadratically as a function of the convective updraft fraction in the global non-hydrostatic Model for Prediction Across Scales (MPAS). We evaluated the performance of GF using quasi-uniform meshes and a variable-resolution mesh centered over South America which resolution varied between hydrostatic (50 km) and nonhydrostatic (3 km) scales. Four-day forecasts using a 50 km and a 15 km quasi-uniform mesh, initialized with GFS data for 0000 UTC 10 January 2014, reveal that MPAS overestimates precipitation in the tropics relative to the Tropical Rainfall Measuring Mission Precipitation Analysis data. Results of four-day forecasts using the variable-resolution mesh reveal that over the refined region of the mesh, GF performs as a precipitating shallow convective scheme whereas over the coarse region of the mesh GF acts as a conventional deep convective scheme. As horizontal resolution increases and subgrid scale motions become increasingly resolved, the contribution of convective and grid-scale precipitation to the total precipitation decreases and increases, respectively. Probability density distributions of precipitation highlight a smooth transition in the partitioning between convective and grid-scale precipitation, including at gray-zone scales across the transition region between the coarsest and finest regions of the global mesh. Variable-resolution meshes spanning between hydrostatic and nonhydrostatic scales are shown to be ideal tools to evaluate the horizontal scale dependence of parameterized convective and grid-scale moist processes.

1. Introduction

In atmospheric modeling systems, the choice of horizontal resolution drives moist processes and precipitation to be classified as implicitly represented using convective parameterizations or explicitly simulated using cloud microphysics parameterizations. At low horizontal resolutions, it is expected that the parameterized convective transport and precipitation contribute a major part to the total transport and precipitation. At high horizontal resolutions, the effect of parameterized convection is expected to weaken as subgrid-scale motions become better resolved and dominate the total transport and precipitation.

Parameterizations of moist convection (e.g. Arakawa and Schubert 1974; Grell 1993; Kain and Fritsch 1993; Tiedtke 1989) were originally developed for atmospheric modeling systems where horizontal resolutions were too coarse to explicitly simulate convective motions. In these so-called conventional mass-flux schemes, the formulation of the vertical convective eddy transport as a function of the cloud mass flux relies on the assumptions that the area occupied by convective updrafts is very small relative to that of the model grid box and that the mean vertical velocity is several times smaller than the vertical velocity of individual convective updrafts. As the horizontal resolution of global numerical prediction systems moves towards non-hydrostatic scales (Satoh et al. 2008; Yeh et al. 2002; Skamarock et al. 2012), these fundamental assumptions break down and a spatial scale dependence of the vertical convective eddy transport is required.

Arakawa et al. (A11; 2011), followed by Arakawa and Wu (A13; 2013), introduced the concept of a *unified* parameterization of convection for use at all horizontal scales between those used in low-resolution global circulation models (GCMs) and those used in cloud-scale resolving models (CRMs). A13 demonstrated that as horizontal resolution increases and the fractional area covered by convective updrafts increases, the vertical convective eddy transport decreases relative to that calculated with full adjustment to a quasi-equilibrium state in conventional mass-flux schemes, and that the scaling factor between the reduced eddy transport and that with full adjustment is a quadratic function of the convective updraft fraction. The quadratic dependence of the vertical convective eddy transport on the convective updraft fraction ensures a smooth transition in the calculation of subgrid-scale convective motions across scales, including the so-called "gray scales" at which conventional convective parameterizations are ill-posed.

Several studies addressed the dependence of mass-flux based convective parameterizations on spatial resolution and new approaches have been implemented to simulate convection at all scales in numerical weather prediction (NWP) models (e.g. Kuell et al. 2007; Gerard et al. 2009; Gomes and Chou 2010; Grell and Freitas 2014). Kuell et al. (2007) argued that the assumption of the updraft, downdraft, and environmental subsidence mass fluxes to be confined in one grid column breaks down in NWP models with horizontal resolution of a few kilometers. Instead, their *hybrid* approach assumes that convective updrafts and downdrafts can remain parameterized in the local grid-column while environmental subsidence can spread to neighboring columns and be treated by the grid-scale equations at increased horizontal resolutions. Gerard et al. (2009) introduced a prognostic treatment of the convective updraft and downdraft fractions and increased interactions between convective and grid-scale condensation to reduce the intermittent on and off behavior of deep convection and biases in the diurnal cycle of convective precipitation (Guichard et al. 2004) when conventional mass-flux schemes are used at finer resolution and smaller time-steps. Gomes and Chou (2010) analyzed the horizontal scale dependence of the partitioning between convective and grid-scale precipitation in the Eta model (Mesinger et al. 1998) at different horizontal resolutions. The Eta model used the Kain-Fritsch (KF, Kain 2004) and Ferrier (Ferrier et al. 2002) parameterizations to simulate convective and cloud microphysics processes, respectively. Their results from multi-day forecasts over the South Atlantic Convergence Zone are opposite to what is expected as horizontal resolutions increase, for convective precipitation increases and grid-scale precipitation decreases as grid sizes decrease. Gomes and Chou (2010) improved the scale dependence of convective and grid-scale precipitation by adding a resolution-dependent parameter in KF that lets a fraction of the convective in-cloud condensate to evaporate and increase environmental moisture. Grell and Freitas (2014) introduced a revised version of the stochastic convection parameterization developed by Grell and Devenyi (2002) that includes a simple implementation of the ideas first proposed in A11. The parameterization is simply referred to as GF in this study. Experiments run with the Brazilian developments on the Regional Atmospheric Modeling System (BRAMS, Freitas et al., 2009) using GF over South America for horizontal resolutions ranging from 20 km to 5 km showed that parameterized convective heating and drying rates become smaller as horizontal resolution increases and that parameterized convection is turned off completely at the highest resolutions. GF is currently used operationally in the Rapid Refresh model system (RAP, Benjamin et al. 2015) at the National Centers for Environmental Prediction.

Alternatives to using spatially-uniform CRMs and high-resolution GCMs to investigate the partitioning between implicit and explicit vertical eddy transport and precipitation with varying horizontal resolutions are variable-resolution GCMs with enhanced horizontal resolution over specific regions, such as stretched grid GCMs (Fox-Rabinovitz et al. 2000), the Ocean Land Atmosphere model (Walko and Avissar 2008), and unstructured grid GCMs such as the Model for Prediction Across Scales (MPAS; Skamarock et al. 2012). MPAS is a fully compressible non-hydrostatic GCM developed for numerical weather prediction and climate applications. MPAS uses an unstructured Spherical Centroidal Voronoi Tesselation (SCVT) for its horizontal grid, and its geometrical properties are well suited to global and regional atmospheric modeling as discussed by Ju et al. (2011) and Ringler et al. (2008). In addition to providing global quasi-uniform resolution meshes, SCVT generation algorithms provide the means to create variable-resolution meshes through the use of a single scalar density function, hence opening opportunities for regional downscaling and upscaling between meso-scales and non-hydrostatic scales to hydrostatic scales within a global framework. MPAS has been extensively tested using idealized cases such as the baroclinic wave test case of Jablonowski and Williamson (Park et al., 2013), and 10-day global forecasts with full physics (Skamarock et al., 2012) to assess the robustness of the dynamical solver for quasi-uniform and variable-resolution meshes. Results from multiple configurations of MPAS verify that smooth transitions between the fine- and coarse-resolution regions of the mesh lead to no significant distortions of the atmospheric flow.

We have implemented the GF scale-aware convection parameterization in MPAS. We have tested the performance of GF to simulate precipitation against observations at hydrostatic scales using quasi-uniform meshes. Furthermore, we have tested the impact of the horizontal resolution dependence of the convective updraft fraction on the partitioning between convective and grid-scale precipitation using a variable-resolution mesh which horizontal resolution varies between hydrostatic scales in the coarsest region of the mesh to non-hydrostatic scales in the most refined region of the mesh. In Section 2, we summarize the chief characteristics of GF and briefly describe the MPAS dynamical core, including its physics components. In Section 3, we describe the different experiments run with the quasi-uniform and variable-resolution meshes. Results using the quasi-uniform mesh are discussed in Section 4 while results using the variable-resolution mesh are described in Section 5. In Section 6, we discuss the impact of GF on the temperature and zonal wind profiles over the refined region of the mesh, as a way to illustrate the possible impact of a scale dependent parameterization of convection on the regional atmospheric circulation. In Section 7, we summarize our results and outline avenues of future research.

2. The convective parameterization

The GF parameterization of convection is described in detail in Grell and Freitas (2014). It is based on the parameterization initially developed by Grell (1993) and further expanded by Grell and Devenyi (2002) to include stochasticism. What distinguishes GF from its preceding versions is the inclusion of the unified parameterization of deep convection first proposed by A11, and described in detail in A13 and Wu and Arakawa (W14; 2014) to calculate the convective vertical eddy transport of moist static energy, moisture, and other intensive variables at varying horizontal scales. A13 demonstrates that mass-flux-based parameterizations of convection developed for low horizontal resolution GCMs can be modified to work at all horizontal grid scales through the reduction of the convective vertical eddy transport as a function of the horizontal fraction of the GCM grid-box occupied by convective updrafts, or convective updraft fraction σ. Importantly, A13 ensures that the formulation of the vertical convective eddy transport reduces to that used in conventional convective parameterizations with full quasi-equilibrium adjustment as σ becomes small relative to the size of individuals GCM grid-boxes. A13 formulates the vertical convective eddy transport $\overline{w'\psi'}$ of an intensive variable ψ as

$$\overline{w'\psi'} = (1-\sigma)^2 \left(\overline{w'\psi'}\right)_E \qquad (1)$$

where w is the vertical velocity and $\left(\overline{w'\psi'}\right)_E$ is the convective vertical eddy transport under full quasi-equilibrium adjustment. In A13, σ is calculated as

$$\sigma = \frac{\left(\overline{w'\psi'}\right)_E}{\Delta w \Delta \psi + \left(\overline{w'\psi'}\right)_E} \qquad (2)$$

to ensure computational stability under all atmospheric conditions. In Eq. (2), Δw and $\Delta \psi$ are differences in w and ψ between the convective updraft and the environment.

As stated in Grell and Freitas (2014), “different closures may be available for the fractional coverage of updraft and downdraft plume”. Because the original intent was to keep GF as simple as possible while retaining a smooth transition between hydrostatic and non-hydrostatic scales, GF choose to follow the traditional entrainment hypothesis of Simpson et al. (1965). GF specifies σ as a function of the half-width radius of the convective updrafts, *R*, as defined in Simpson and Wiggert (1969), or

$$\sigma = \frac{\pi R^2}{A} \text{ and } R = \frac{0.2}{\varepsilon} \text{ .} \tag{3}$$

In Eq. (3), A is the area of the grid-box and ε is an initial fractional entrainment rate set to 7x10-5 per meter. This formulation causes significant scale adjustment starting at about 20 km horizontal grid size. In addition, GF assumes that σ is limited to a maximum value σ_{max}. When σ exceeds σ_{max}, the convective parameterization can either be turned off, or as is done in BRAMS, RAP, and our experiments for smaller values of A, σ can be set to σ_{max} and ε recalculated using Eq. (3), leading to increased values of ε for a given A. This will lead to a decrease in cloud top height as resolution is increased further. σ_{max} is set to 0.7 for this approach (starting the transition to more shallow convection at a horizontal resolution of approximately 6 km). If the preferred choice is to turn off the convective parameterization, a better value for σ_{max} may be between 0.9 and 1. Relative to Eq. (2), Eq. (3) implies that σ is independent of height. As shown in W14 (see their Fig. 1), there is almost no dependence of σ as a function of height for domain sizes ranging between 64 km and 2 km, at least from idealized experiments using a CRM. Therefore, using Eq. (3) is a reasonable simplification of the full procedure proposed by A13 for practical applications. As we focus our results on the response of GF to horizontally varying scales, the vertical dependence of σ is beyond the scope of this study.

Conventional mass-flux parameterizations of deep convection assume that vertical velocities inside convective updrafts are several orders of magnitude greater than environmental vertical velocities. Under that assumption, it can be shown that $\left(\overline{w'\psi'}\right)_E$ can be written as

$$\left(\overline{w'\psi'}\right)_E \approx \sigma w_c \Delta\psi = \frac{M_E}{\rho_a}\Delta\psi \qquad (4)$$

where M_E is the updraft mass flux per unit area, ρ_a is the air density, w_c is the vertical velocity inside the updraft, and $\Delta\psi$ is the difference in ψ between the updraft and the environment. In Eq. (4), variables are defined at a given height z inside the convective updraft. It is normal practice to further express $M_E(z)$ as a function of the cloud base mass flux per unit area, M_B, or

$$M_E(z) = M_B \eta(z) \qquad (5)$$

Where $\eta(z)$ is the entrainment rate. Using Eqs. (4) and (5) in Eq. (1), we get

$$\overline{w'\psi'}(z) = (1-\sigma)^2 M_B \frac{\eta(z)}{\rho_a(z)}\Delta\psi(z) \ . \qquad (6)$$

GF uses a variety of closures to determine M_B and solve Eq. (6) as described in Grell and Freitas (2014). Because σ is independent of height, implementing the horizontal scale dependence of A13 in GF reduces to weighting M_B by $(1-\sigma)^2$ and thus requires few modifications to the original scheme.

We implemented and tested the GF scheme using MPAS. The nonhydrostatic dynamical core in MPAS is described in Skamarock et al. (2012). It solves prognostic equations for the horizontal momentum (cast in vector-invariant form), vertical velocity, potential temperature, dry air density, and scalars. The prognostic equations are cast in flux form to ensure conservation of first-order quantities (e.g. dry-air mass, scalar mass, and entropy). The horizontal discretization uses a C-staggering of the prognostic variables on a horizontal mesh as described in Ringler et al. (2010). The vertical discretization uses the height-based hybrid terrain-following coordinate of Klemp (2011) in which coordinate surfaces are progressively smoothed with height to remove the impact of small-scale terrain structures. The dynamical solver integrates the flux-form compressible equations using the split-explicit technique described in Klemp et al. (2007). The basic temporal discretization uses the third-order Runge-Kutta scheme and explicit time-splitting technique described in Wicker and Skamarock (2002). MPAS uses the scalar transport scheme described in Skamarock and Gassman (2011) on the Voronoi mesh, and the monotonic option is used for all moist species. Finally, MPAS uses the horizontal filtering of Smagorinsky (1963) as described in Skamarock et al. (2012).

In addition to GF, the suite of physics parameterizations includes

- the land-surface parameterization described by Chen and Dudhia (2001),
- the Mellor-Yamada-Nakanishi-Niino planetary boundary layer and surface-layer schemes described by Nakanishi and Niino (2009),
- the cloud microphysics parameterization of Hong and Lim (WSM6, 2006),
- the Kain-Fritsch (KF; Kain 2004, Kain and Fritsch 1993) parameterization of convection,
- the Tiedtke (TD; Tiedtke 1989) parameterization of convection,
- the semi-empirical cloudiness parameterization of Xu and Randall (1996), and,
- the Rapid Radiation Transfer Model for application to GCMs described by Mlawer et al. (1997) and Iacono et al. (2000).

3. Description of numerical experiments

Prior to listing the series of experiments run to test GF, we describe the characteristics of the variable-resolution mesh centered at 4°S-63°W. This mesh, hereafter labeled as the 50-3 mesh, is the mesh we used to investigate the response of GF at scales varying between the hydrostatic and non-hydrostatic regimes with MPAS. Figure 1.a displays black isolines of the mean distance between cell centers and color-filled contours of σ. The variable-resolution region has a circular structure and the most refined region of the mesh, i.e. area with a distance between cell-centers less than 6 km, encompasses most of South America and expands east and west over the Atlantic and Pacific Oceans. Figure 1.a also shows that there exists a smooth transition between the finest and coarsest region of the mesh with the distance between the 6 km and 24 km isolines spanning over 3300 km along the equator. Figure 1.b displays a histogram of the mean distance between cell centers. As shown in Table 1, the minimum and maximum distances between cell centers are 2.2 km and 60.2 km, respectively. 67% of the 6,848,514 cells have a mean distance between cell centers less than 4 km whereas only 3.6% have a mean distance between cell centers greater than 20 km. The number of cells with mean distances greater than 4 km decreases very rapidly and reaches a minimum for distances greater than 20 km, except for the bin between 40 km and 50 km. Figure 1.c highlights the rapid decrease in σ from σ_{max} to 0.3 as the mean distance between cell centers increases only from 6.1 km to 9.2 km. σ further decreases from 0.3 to 0.1 for distances between 9.2 km and 16 km. Finally, σ decreases slowly from 0.1 to 0.01 for a wide range of distances spanning between 16 km and 50 km. As discussed in GF14, Fig. 1.c shows that $(1-\sigma)^2$ decreases rapidly as spatial resolution increases and that its impact on the cloud base mass flux becomes significant for mean distances between cell centers less than 20 km.

In order to test the performance of GF at various horizontal resolutions, we ran four four-day forecasts (QU50, NS50, QU15, and NS15) with a quasi-uniform mesh and three four-day forecasts (GF70, GFNS, and NOGF) with the 50-3 mesh described above. In QU50 and NS50, the mean distance between cell centers is approximately equal to 50 km and the number of cells is 256,002. In QU15 and NS15, the mean distance between cell centers is approximately equal to 15 km and the number of cells is equal to 2,621,442. In QU50 and QU15, σ is computed using Eq. (3), and is equal to 0.01 and 0.11, respectively. In NS50 and NS15, σ is equal to 0 to remove the horizontal resolution dependence on the calculation of $\left(\overline{w'\psi'}\right)$. Our motivation for QU50 and QU15, and NS50 and NS15, is to assess the performance GF in MPAS at hydrostatic scales.

All three experiments GF70, GFNS, and NOGF use the 50-3 mesh. In GF70, we set the maximum convective cloud fraction $\sigma_{\max}$ to 0.7 and adjusted the initial entrainment rate accordingly. In order to test the scale sensitivity of GF to horizontal resolution inside and outside the region of mesh refinement, we set σ equal to 0 in GFNS as in NS50 and NS15 while we turned off GF in NOGF. All experiments are initialized using analyses from the Global Forecast System (GFS) for 0000 UTC 10 January 2014. Additional details pertinent to the experiments are summarized in Table 1.

4. Results with the quasi-uniform mesh

Figure 2 shows the distribution of daily mean precipitation rates calculated between 0000 UTC 11 January 2014 and 0000 UTC 14 January 2014. The top left panel displays observed precipitation rates from the Tropical Rainfall Measuring Mission (TRMM) Precipitation Analysis (TMPA Version 7; Huffman et al. 2010). The top right panel shows precipitation rates from the GFS three-day forecast initialized on 0000 UTC 11 January 2014, and available on a 0.50°x0.50° latitude-longitude. The bottom left and right panels display precipitation rates from QU50 and QU15. We allowed MPAS to spin up for one full day past the initial conditions. Simulated and observed precipitation rates are displayed using their respective horizontal resolutions. Precipitation rates spatially-averaged between 50°N-50°S for QU50, QU15, TMPA data, and the GFS forecast are summarized in Table 2.

TMPA data display areas of highest precipitation over the well-known convectively active regions over land and oceans in January. Over oceans, these regions include the Inter-Tropical Convergence Zone (ITCZ) located between the Equator and 10°N across the tropical Eastern Pacific and Atlantic Oceans, the South Pacific and South Atlantic Convergence Zones, a major part of the Indian Ocean, and the so called warm pool region over the tropical Western Pacific Ocean. Over land, convectively active regions comprise a major part of South America between the Equator and 10°S, and Southern Africa. In the middle latitudes, TMPA data show areas of highest precipitation in the middle of the subtropical Atlantic Ocean, over the eastern United States, and along the eastern coast of North America over the Atlantic Ocean. At a 0.25°x0.25° latitude-longitude resolution, TMPA data reveal strong gradients between adjacent areas of strong and weak precipitation, highlighting the strong spatial and temporal variability of precipitation.

There exist significant differences between the GFS precipitation and TMPA data over land and oceans. Over South America and Southern Africa, the GFS forecast underestimates the spatial extent of highest precipitation rates. Decreased precipitation is also observed over the eastern United States and along the eastern coast of North America over the Atlantic Ocean. In the subtropics, the GFS forecast leads to increased precipitation over the subtropical Pacific and Atlantic Oceans. Decreased precipitation over land contributes a major part to the 0.4 mm day^{-1} negative bias in the 50°N-50°S spatially-averaged precipitation rates between the GFS forecast and TMPA data.

Figure 2 shows that while simulating reasonably well the main areas of highest precipitation, QU50 and QU15 systematically overestimate precipitation over convectively active regions in the tropics when compared against the TMPA data and the GFS forecast. Increased precipitation is obvious over South America, Southern Africa, the western Indian Ocean, and the warm pool region, particularly in QU50. Both QU50 and QU15 overestimate (underestimate) the strength of the ITCZ along the eastern Pacific (Atlantic) Ocean. As in the GFS forecast, QU50 and QU15 underestimate precipitation over the eastern United States and the eastern coast of North America. QU50, QU15, and GFS also overestimate precipitation over the subtropical oceans, as seen over the South Pacific and South Atlantic Oceans.

In Fig. 3, we show zonal mean differences in the precipitation rates between QU50, QU15, and TMPA data, and between the GFS forecast. Outside of the latitudinal belt between 15°N and 15°S, differences against the GFS forecast oscillate between plus and minus 0.8 mm day^{-1} while differences against TMPA data are mostly positive and exceed 1.0 mm day^{-1}. This result corroborates that, at extra tropical latitudes, QU50, QU15, and the GFS forecasts produce similar biases when compared against TMPA data, namely increased precipitation over the subtropical oceans and decreased precipitation over the eastern United States and along the east coast of North America. Between 15°N and 15°S, zonal mean differences are mostly positive and have absolute values greater than 3.4 mm day^{-1} when compared against both the TMPA data and GFS forecast. This result suggests that the GFS forecast is in better agreement than QU50 and QU15 when compared against TMPA data over convectively active regions in the tropics. The maximum zonal mean bias located around 10°S decreases slightly in QU15 relative to QU50 in response to increased spatial resolution. As seen in Table 2, the bias in the 50°N-50°S spatially-averaged precipitation rate decreases from 0.4 mm day^{-1} between the GFS forecast and TMPA data to 0.2 mm day^{-1} between the TMPA data and both QU50, QU15. However, this decreased bias is a result of compensating positive biases in the tropics and negative biases in the extra tropics.

In order to get an initial insight into the origins of increased precipitation in QU50 and QU15 in the tropics, we replaced GF with the cumulus parameterizations developed by Kain and Fritsch (Kain 2004) and Tiedtke (1989) and ran the experiments KF50, TD50, KF15, and TD15 using the 50 km and 15 km quasi-uniform meshes. Comparing precipitation rates obtained with KF50, KF15, TD50, and TD15 against TMPA data and the GFS forecast show differences that have similar geographical patterns and magnitude as the ones shown in Figs. 2 and 3. These results are not shown here for brevity. Table 2 shows that the 50°N-50°S spatially-averaged precipitation rates obtained with KF50, KF15, and TD15 are close to the ones obtained with QU50 and QU15 while that obtained with TD50 is 0.46 mm day^{-1} greater than observed. Given that all three parameterizations yield increased precipitation over land and oceans in the tropics, we infer that interactions between the convective and other physics parameterizations, in particular cloud microphysics and radiation, are responsible for the biases outlined above. Origins of these discrepancies and improvement of GF within the MPAS modeling framework will be the focus of future research.

Figure 4 displays the geographical distributions of the convective and grid-scale precipitation rates obtained with QU50 and QU15 over the same time period as the total precipitation rates shown in Fig. 3. As seen in Fig. 4, convective precipitation contributes a major part to the total precipitation in the tropics over land and oceans. Grid-scale precipitation contributes the major part to the total precipitation in the extra-tropics. As seen in the bottom panels of Fig. 4, grid-scale processes are responsible for increased precipitation relative to TMPA data over the subtropical oceans. Table 3 summarizes the global mean precipitation rates for the different experiments. The global mean decrease in total precipitation between QU50 and QU15 is only 0.07 mm day^{-1} and results from a 0.21 mm day^{-1} decrease in convective precipitation compared to a 0.14 mm day^{-1} increase in grid-scale precipitation. Geographical distributions of differences in total, convective, and grid-scale precipitation between QU50 and QU15 would show that the impact of increased resolution is highly variable with areas of increased total precipitation closely neighboring areas of decreased precipitation (not shown for brevity). The decrease in convective precipitation in QU15 relative to QU50 occurs over every convectively active areas in the tropics over both land and oceans. The increase in grid-scale precipitation is noisy and confined over small areas such as the northern coast of Australia, the Philippines, and the equatorial Atlantic Ocean. Despite the fact that GF includes a horizontal resolution dependence on the cloud base mass flux and TD does not, the decrease in convective and total precipitation and compensating increase in grid-scale precipitation is more than twice as large in TD than in GF. The change in convective, grid-scale, and total precipitation is about the same in KF as in GF.

Finally, we analyze the impact of including or not including the $(1-\sigma)^2$ scaling of the updraft mass flux by comparing QU50 and QU15 against NS50 and NS15, respectively. In NS50 and NS15, we removed the resolution dependence of GF by setting $(1-\sigma)^2$ to 1 in Eq. (6). As listed in Table 1, $(1-\sigma)^2$ is equal to 0.980 in QU50 and decreases to 0.785 in QU15. Figure 5 displays the zonal mean differences in the convective, grid-scale, and total precipitation rates between QU50 and NS50, and between QU15 and NS15. As $(1-\sigma)^2$ is near 1 in QU50, we do not expect large differences in the accumulated precipitation when compared against NS50. Indeed, outside of a few latitude bands, Fig. 5.a shows zonal mean differences in convective precipitation less than 0.4 mm day^{-1}, confirming that GF acts as a conventional cloud-base mass flux parameterization at hydrostatic scales. Table 3 shows that global mean convective, grid-scale, and total precipitation rates are nearly the same in QU50 and NS50. As spatial resolution increases from hydrostatic to non-hydrostatic resolution, the impact of weighting the cloud base mass flux by $(1-\sigma)^2$ increases. Figure 5.b shows that between 30°N and 30°S convective precipitation rates decrease while grid-scale precipitation rates increase in response to the reduced convective mass flux. As the change in grid-scale precipitation does not balance exactly that in the convective precipitation, the total precipitation decreases with increased spatial resolution. As listed in Table 3, there is a 0.05 mm day^{-1} decrease in total precipitation between NS15 and QU15 and a near cancellation between the decreased convective precipitation (-0.17 mm day^{-1}) and increased grid-scale precipitation rate (0.12 mm day^{-1}).

5. Results with the variable-resolution mesh

a. *Precipitation rates*

Figures 6, 7, and 8 show the global distribution of convective, grid-scale, and total precipitation rates averaged between 0000 UTC 11 January 2014 and 0000 UTC 14 January 2014 and simulated in GF70, GFNS, and NOGF. Comparing the convective precipitation rate simulated in GF70 against that obtained in GFNS inside and outside the area of mesh refinement clearly highlights the impact of the scale dependence of the cloud mass flux as a function of the convective updraft fraction in GF. A comparison between Figs. 6.a and 6.b shows significantly decreased convective precipitation over the regions where σ increases towards $\sigma_{\max}$ over South America, the tropical Eastern Pacific Ocean east of 110°W, and a major portion of the Western Atlantic Ocean between 40°N and 40°S. Outside these regions, the magnitude and patterns of convective precipitation in convectively active regions over land and oceans in the tropics are similar, except for differences inherent to expected variability between the two experiments. In GF70, increased grid-scale precipitation compensates decreased convective precipitation over the area of mesh refinement such that it resembles that obtained in NOGF, as shown in Figs. 7.a and 7.c. In contrast, convective precipitation exceeds grid-scale precipitation outside the refined mesh such that it resembles that obtained in GFNS. Inside the area where σ equals 0.7, the region with 3 km mean distance between grid-cell centers yields a strong spatial variability in accumulated grid-scale precipitation in both GF70 and NOGF relative to that observed in the coarser area of the mesh over the extra-tropics. Figure 7.b shows that grid-scale precipitation is strongly reduced in GFNS relative to that simulated in GF70 and NOGF over the area of local mesh refinement over South America and the ITCZ over the tropical Eastern Pacific and Western Atlantic Oceans. In GFNS, setting σ equals 0 results in GF to behave as if the mesh was a quasi-uniform instead of a variable-resolution mesh and for subgrid-scale convective processes to dominate cloud microphysics processes over convectively active regions in the tropics, as discussed for the quasi-uniform experiments in Section 4.

In term of total precipitation, Fig. 8 shows that the GF70 forecast has magnitudes and patterns similar to the ones obtained with NOGF and GFNS inside and outside the refined area of mesh, respectively. Over the area where σ equals 0.7, GFNS overestimates total precipitation relative to GF70 and NOGF; GF does not respond to increased spatial resolution and subgrid-scale convective processes contribute a major part to the total precipitation. In contrast, GF70 displays smaller total precipitation differences relative to NOGF than GFNS as parameterized deep convection strongly weakens and GF transitions from a deep convection to a shallow precipitating convection scheme. Over the coarse area of the mesh where σ decreases to 0.01, the total precipitation from GF70 and GFNS significantly exceeds that from NOGF, as seen over the main convectively active regions over land and oceans. The need for parameterized convection at hydrostatic scales is obvious when comparing NOGF against GF70 and GFNS, and NOGF against TMPA satellite data shown in Fig. 2.a. Over the coarsest region of the mesh, the geographical distribution of grid-scale precipitation is noisy over convectively active regions. Over the subtropical Pacific and Atlantic Oceans, grid-scale precipitation in NOGF is increased relative to the total precipitation in GF70 and GFNS.

In Fig. 9, we compare the probability density functions (PDFs) of the convective, grid-scale, and total precipitation rates between GF70 and GFNS as functions of three σ intervals. σ varying between 0.7 and 0.5 corresponds to mean distances between grid-cell centers increasing from 3 km to 7 km, including the most refined region of the mesh. σ varying between 0.5 and 0.1 covers the transition zone between the most refined and coarse regions of the mesh with distances between cell centers between 7 and 16 km, including the gray-zone scale. Finally, σ less than 0.1 includes the coarsest region of the mesh where parameterized convection dominates grid-scale processes. The PDFs include data for all the grid cells located between 30°S and 10°N. In GF70, the magnitude and range of convective precipitation gradually become larger as σ becomes smaller. This is indicative of a smooth increase in the impact of parameterized convection between the refined and coarse regions of the mesh. Differences in the range and magnitude of convective precipitation between GF70 and GFNS over the refined region reflect of the inability of the convective parameterization to self-adjust at increased horizontal resolutions when σ equals 0. Both GF70 and GFNS lead to identical PDFs of convective precipitation over the transition and coarse areas of the mesh, indicating that GF rapidly loses its σ dependence as horizontal resolution decreases. The range and magnitude of grid-scale and total precipitation do not counter balance those of convective precipitation in GF70 except over the refined region. Figure 9.b highlights the increase in grid-scale precipitation over the refined are of the mesh between GF70 and GFNS, in response to decreased convective precipitation between the two experiments. Looking at the PDF of total precipitation (Fig. 9.c) reveals that the compensating increased grid-scale precipitation leads to greater magnitude and range of total precipitation in GF70 relative to GFNS. In contrast to convective precipitation, the magnitude and range of grid-scale and total precipitation increase in GF70 relative to GFNS over the transition zone between hydrostatic and non-hydrostatic scales. The PDFs of grid-scale and total precipitation are the same over the coarsest region of the mesh. These results highlight the sensitivity of grid-scale precipitation to horizontal scales as soon as its contribution to total precipitation dominates.

Simulating the diurnal cycle of tropical convection over land is of major importance in NWP forecasts because of its impact on the top-of-the-atmosphere and surface radiation budgets and surface temperatures through the development of convective clouds and precipitation. Using high-resolution TRMM precipitation radar (PR2A25) data between 10°N and 10°S, Takayabu (2002) shows that convective rain shows a 0.25 mm hr^{-1} maximum over land in the 15-18 Local Time (LT) afternoon window while stratiform rain displays a 0.1 mm hr^{-1} midnight (24-03LT) maximum.

Figure 10 displays the diurnal cycle of total precipitation averaged between 15°S-10°N and 80°W-40°W for GF70, GFNS, and NOGF. The observed diurnal cycle is calculated using TMPA data as in Section 4. The data is available eight times per day, averaged over a three-hour time window, and has a 0.25°x0.25° latitude-longitude resolution. The observed diurnal cycle displays two separate maxima of similar magnitude, a night time maximum at 06 UTC (about 02 LT in the center of the area) and a late afternoon maximum at 21 UTC (about 17 LT), in conjunction with the development of afternoon convection and rain showers. Despite its lower temporal spatial resolution relative to PR2A25 data, TMPA data provides a reliable reference against our experiments. As shown in Fig. 10, NOGF and GF70 display a weak early morning maximum at 08 UTC and 09 UTC and a strong mid afternoon maximum at 16 UTC and 19 UTC, respectively. Simulated afternoon maxima are too strong and too early against that from TMPA data. Although the contribution of parameterized convection is strongly reduced relative to that of grid-scale cloud microphysics over the refined region of the mesh, Fig. 10 highlights its positive effect on simulating afternoon convection. Including GF leads to a decreased afternoon maximum that occurs later in GF70 relative to NOGF. Removing the scale-aware dependence of GF worsens the simulation of afternoon convection relative to TMPA. While the diurnal cycle of precipitation simulated with GFNS matches that of TMPA between 03 UTC and 12 UTC, GFNS leads to an unrealistic double peak in precipitation over the second half of the diurnal cycle. In view of our results, it is obvious that σ must be greater than zero. It is not known if allowing σ to be greater than 0.7 would further decrease and delay the afternoon maximum in precipitation in GF70 relative to TMPA.

b. *Tendencies*

This section focuses on the σ dependence of convective and grid-scale temperature and water vapor tendencies, cloud water and cloud ice mixing ratios, and horizontal cloud fraction. Figure 11 displays the vertical distributions of time- and area-averaged convective, grid-scale, and convective plus grid-scale tendencies of temperature (left panels) and water vapor (right panels) from GF70, GFNS, and NOGF. In Fig. 11.d to Fig. 11.f, we multiplied the tendencies of water vapor by L_v over c_p in order to express them with the same unit as the tendencies of temperature in Fig. 11.a to Fig. 11.c. L_v is the latent heat of condensation and c_p is the specific heat of dry air. Convective tendencies include the parameterized vertical eddy transport plus condensation from the convective plume model. The time average is calculated between 0000 UTC 11 January 2014 and 0000 UTC 14 January 2014. As 11 January 2014 is three days past the initial conditions, it is reasonable to assume that the experiments are beyond their spin-up period and comparing time-averaged diagnostics between the three experiments yields an actual depiction of interactions between dynamics and physics processes. The area average is calculated between 15°S and 5°S and 50°W and 65°W, as shown in Fig. 1. The area includes 244,178 cells and is located over the most refined region of the mesh. As seen in Fig. 6, vertical profiles are spatially averaged over an area of minimum convective precipitation from GF70 and maximum convective precipitation in GFNS to highlight the impact of the σ-dependent closure assumption in GF on the partitioning between convective and grid-scale tendencies.

GFNS produces vertical profiles of convective heating and moistening rates characteristic of profiles obtained with mass-flux based parameterizations of deep convection. As shown in Figs. 11.a and 11.d, convective heating and drying occur through the entire atmospheric column above 925 hPa. Convective heating is maximum at 450 hPa. Below 925 hPa, convective tendencies of temperature and water vapor are both negative, and the level at which the convective heating is equal to zero coincides with that at which convective drying is maximum. Finally, detrainment of cloud water and ice at the tops of convective updrafts (not shown) increases with height above 800 hPa reaching a maximum at about 300 hPa. As noted earlier in this section when describing global patterns of convective and grid-scale precipitation, subgrid-scale convective processes dominate grid-scale processes in the tropics. As a result, grid-scale tendencies of temperature and water vapor in GFNS are much smaller than their respective convective tendencies, as seen in Figs. 11.b and 11.e. Figure 11.b (11.e) also reveals a small maximum in grid-scale evaporation (moistening) at 500 hPa and a small maximum in grid-scale condensation (drying) in the layers of increased convective detrainment around 300 hPa.

Multiplying the convective mass flux calculated under the QE assumption by $\left(1-\sigma\right)^2$ has a strong impact on the vertical profiles of convective tendencies over the most refined area of the mesh. As seen in Figs. 11.a and 11.d, GF70 yields vertical profiles of convective heating and moistening that are strongly reduced relative to those obtained with GFNS. The chief differences between GF70 and GFNS include a decrease in convective heating through the entire atmosphere, including a decrease from 9 to less than 1 K day^{-1} at 450 hPa, and the occurrence of a 1.5 K day^{-1} maximum in convective heating at 850 hPa. As shown in Fig. 11.d, reduced deep convection yields not only decreased convective drying at 900 hPa but also increased convective moistening of the middle troposphere between 800 hPa and 500 hPa. This increased convective moistening occurs at parameterized cloud top levels in response to the increased entrainment. In short, reducing the cloud mass flux as a function of the convective updraft fraction leads GF to transition from a parameterization of deep convection to that of precipitating shallow convection as the convective updraft fraction increases over the most refined region of the mesh. Over the refined area of the mesh, compensating effects between cloud microphysics and convective processes yield vertical profiles of grid-scale heating and moistening rates from GF70 similar to those obtained with NOGF, as seen in Figs. 11.b and 11.e. Figures 11.c and 11.f show that the convective plus grid-scale temperature and water vapor tendencies from GF70 and NOGF are very similar, particularly the heating rate. In contrast, the inability of GFNS to adapt to variations in horizontal resolutions yields increased total heating at 450 hPa and increased total drying at 900 hPa relative to GF70 and NOGF.

Finally, Fig. 12 shows the vertical distribution of the resolved cloud water and cloud ice mixing ratios, and horizontal cloud fraction, averaged over the same time interval and area as the tendencies. In GFNS, the major source of cloud water and ice in the tropics is convective detrainment. Fig. 12.a displays a weak maximum in the cloud water mixing ratio at 600 hPa while Fig. 12.b shows a strong maximum in the cloud ice mixing ratio at 300 hPa. The horizontal cloud fraction exhibits a maximum at 200 hPa and rapidly decreases above and below that pressure level as the cloud ice mixing ratio. Atmospheric layers below this level are practically cloud-free between 600 hPa and 900 hPa. In contrast, GF70 exhibits a strong maximum in the cloud water mixing ratio at 600 hPa as deep convection weakens and convective moistening between 500 hPa and 800 hPa strengthens, as depicted in Fig. 11.a. Decreased detrainment of cloud ice at the tops of convective updrafts leads to a decrease in the cloud ice mixing ratio at 200 hPa. GF70 yields a deeper cloud layer than GFNS between 200 hPa and 600 hPa in response to the change in total cloud condensate between the two experiments. As for the convective and grid-scale tendencies, GF70 leads to vertical profiles of the cloud water and ice mixing ratios and of the cloud fraction that are very similar to those from NOGF, as seen in all three panels of Fig. 12. In summary, the σ dependence of the cloud mass flux over the most refined region of the mesh in GF70 yields the formation of a moist layer between 500 hPa and 800 hPa and grid-scale condensation leads to the formation of a cloud layer at mid-tropospheric levels capped by a thinner anvil cloud than in GFNS.

6. Impact on temperature and zonal wind

We discuss the impact of GF on temperature and zonal wind over the refined region of the mesh. The conversion of GF from a parameterization of deep convection to a parameterization of precipitating shallow convection as horizontal resolution increases affects the vertical profile of diabatic heating and therefore temperature. Comparing time- and area-averaged long- and short-wave radiative heating rates between GF70 and GFNS over the same area as in Figs. 11 and 12 would highlight a reduced cooling of the troposphere below 600 hPa and an enhanced cooling of the troposphere above between 600 hPa and 200 hPa (not shown for brevity). It would also be show that long-wave radiation contributes a major part to the change in radiative heating between the two experiments. The redistribution of radiative heating rates between the middle and upper troposphere results because middle-level clouds increase whereas high-level clouds decrease, as previously shown in Fig. 12. Comparing time- and area-averaged diabatic heating rates calculated in GF70 against those in GFNS would reveal an increased cooling below 850 hPa coupled with a decreased warming above 850 hPa (not shown for brevity). In GF70, grid-scale evaporation contributes a major part to the increased cooling relative to GFNS below 850 hPa with maximum cooling occurring at 925 hPa. Between 850 hPa and 200 hPa, combined increased radiative cooling and decreased convective and grid-scale heating lead to a decreased diabatic heating of the upper troposphere.

Figs. 13.a-13.c show differences in temperature between GF70 and GFNS at three pressure levels over the refined and transition regions of the mesh. Although we recognize that there are different convective regimes across South America besides that depicted over the Amazon Basin in Figs. 11 and 12, it appears that the change in diabatic heating with height as discussed above is typical of the impact of GF across most of South America. Temperatures are dominantly colder in GF70 than in GFNS at 850 hPa and 500 hPa and absolute temperature differences between the two experiments decrease with height. At 200 hPa where the impact of the change in the vertical profile of clouds is not as large as at higher pressure levels, absolute temperature differences are smaller, and temperatures are actually warmer in GF70 than in GFNS over part of the continent. Over oceans, GF70 leads to warmer temperatures than GFNS over major cloud systems, as seen over the South Atlantic Convergence Zone and the low-level stratus region off the Peruvian and Chilean coasts. Absolute temperature differences are smaller over oceans than over land because sea-surface temperatures are held fixed, limiting the effect of surface heating on the development of convection in both GF70 and GFNS. As seen in Figs. 13.d-13.f, zonal wind differences vary widely over the refined area of the mesh at all three pressure levels. GF70 leads to predominantly decreased zonal wind at 850 hPa but increased zonal wind at 500 hPa and 200 hPa relative to GFNS over most of the Amazon Basin north of 15°S. Absolute values of zonal wind differences are generally greater in the upper- than lower troposphere. Over the coarse region of the mesh, differences in temperature, zonal wind, and other atmospheric variables such as vertical velocity and relative humidity, remain small as GF70 and GFNS lead to similar diabatic heating profiles as the convective updraft area decreases rapidly relative to the area of the grid-cell.

7. Summary and conclusion

A variable-resolution mesh in which horizontal resolution varies between hydrostatic and non-hydrostatic scales has been used to study the scale dependence of a convective parameterization within a global framework. We implemented the GF parameterization of convection in MPAS to test a formulation of the horizontal scale dependence of the cloud base mass flux as a function of the cloud updraft fraction using quasi-uniform and variable-resolution meshes. We focused on the partitioning between convective and grid-scale precipitation as a function of the cloud updraft fraction, and differences in the vertical distributions of convective and grid-scale tendencies. As horizontal resolution increases from the coarsest to the finest area of the mesh, convective processes transition from parameterized to resolved, and grid-scale precipitation progressively contributes to a major part to the total precipitation.

First, we tested the performance of GF using a 50 km and a 15 km quasi-uniform resolution mesh with and without the scale dependence of the cloud mass flux on the cloud updraft fraction. Our results show that parameterized convective precipitation contributes a major part of the total precipitation in the tropics while grid-scale precipitation contributes a major part of the total precipitation in the extratropics. All four experiments overestimate total precipitation when compared against TMPA data and GFS forecast over land and oceans, particularly in the tropics. Additional experiments in which we replaced GF with KF and TD also lead to increased precipitation in the tropics, leading us to conclude that parameterizations of the interactions between convection and other physics components may be as responsible as any of the three parameterizations of convection to explain this systematic bias. Further analyses will focus on comparing top-of-the-atmosphere and surface radiation budgets against satellite data and GFS analyses to ensure that our forecasts produce realistic interactions between convective, grid-scale, and radiative processes through the parameterization of the grid-scale horizontal cloud fraction and optical properties.

Second, we tested the convective updraft fraction dependence of the cloud mass flux using a variable-resolution mesh centered over South America. Our high-resolution variable-resolution mesh allowed the testing of the GF at all scales spanning between the hydrostatic (50 km) and non-hydrostatic (3 km) regimes. Results showed that as the convective updraft fraction increased and the convective mass flux decreased from the coarsest to the most refined region of the mesh, convective processes weakened whereas grid-scale cloud microphysics processes strengthened. Over the most refined area of the mesh, grid-scale precipitation contributed a major part to total precipitation, and vertical profiles of subgrid-scale convective heating and drying showed that GF behaved as a precipitating shallow convection scheme. The diurnal cycle of precipitation exhibited a primary maximum during the mid afternoon. PDFs of subgrid-scale convective, grid-scale, and total precipitation as functions of the updraft fraction highlighted the smooth transition of subgrid-scale convective precipitation across horizontal scales, including at gray-zone resolutions. As for the quasi- uniform resolution experiments, we will analyze the impact of the change in vertical profiles of the grid-scale cloud water and ice mixing ratios, and the cloud fraction on the top-of-the atmosphere and surface radiation budgets.

We are encouraged by the performance of GF using an unstructured variable-resolution mesh for scale-aware convection simulations at non-hydrostatic scales. Future analyses will evaluate the characteristics of subgrid-scale convective and grid-scale cloud systems, focusing over the finest region of the mesh comparing against TRMM and CloudSat data, as pioneered by Satoh et al. (2010) and Dobson et al. (2013). A newer version of GF is currently being tested in the Weather Research Forecast Model (Skamarock et al. 2008) and includes the diurnal cycle effect (Bechtold et al., 2014) and a coupling with the Stochastic Kinetic-Energy Backscatter Scheme (SKEBS; Berner et al. 2009).

Acknowledgments. The National Center for Atmospheric Research is sponsored by the National Science Foundation (NSF). This research was partially supported by the Disaster Relief Appropriations Act of 2013. Dr. S. R. Freitas acknowledges partial support by FAPESP (2014/01563-1). The TMPA data used in this effort were acquired as part of part the activities of NASA's Science Mission Directorate, and are archived and distributed by the Goddard Earth Sciences (GES) Data and Information Services Center (DISC).

REFERENCES

Arakawa, A., J.-H. Jung, and C.-M Wu, 2011: Toward unification of the multiscale modeling of the atmosphere. *Atmos. Chem. Phys*., **11**, 3731-3742.

Arakawa, A., and W.H. Schubert, 1974: Interaction of a cumulus cloud ensemble with the large-scale environment, Part I. *J. Atmos. Sci.,* **31**, 674-701.

Arakawa, A., and C.-M. Wu, 2013: A unified representation of deep moist convection in numerical modeling of the atmosphere. Part I. *J. Atmos. Sci.,* **70**, 1977-1992.

Bechtold, P., N. Semane, P. Lopez, J.-P. Chaboureau, A. Beljaars, and N. Bormann, 2014: Representing equilibrium and nonequilibrium convection in large-scale models. *J. Atmos. Sci.*, **71**,734-753.

Benjamin, S., S. Weygandt, M. Hu, C. Alexander, T. Smirnova, J. Olson, J. Brown, E. James, D. Dowell, G. Grell, H. Lin, S. Peckham, T. Smith, W. Moninger, and G. Manikin, 2015: A north american hourly assimilation and model forecast cycle: The rapid refresh. *Submitted to Mon. Wea. Rev*.

Berner, J., G.J. Shutts, M. Leutbecher, and T.N. Palmer, 2009: A spectral stochastic kinetic energy backscatter scheme and its impact on flow-dependent predictability in the ECMWF ensemble prediction system. *J. Atmos. Sci*., **66**, 603-626.

Chen, F., and J. Dudhia, 2001: Coupling an advanced land surface-hydrology model with the Penn State-NCAR MM5 modeling system. Part I: Model implementation and sensitivity. *Mon. Wea. Rev*., **129**, 569-585.

Dobson, J.B., D.A. Randall, and K. Suzuki, 2013: Comparison of observed and simulated tropical cumuliform clouds by CloudSat and NICAM. *J. Geophys. Res*., **118**, 1852-1867, doi:10.1002/jgrd.50121.

Ferrier, B.S., Y. Lin, T. Black, E. Rogers, and G. DiMego, 2002: Implementation of a new grid-scale cloud and precipitation scheme in the NCEP Eta model. *19th Conference on Weather Analysis and Forecasting/15th Conference on Numerical Weather Prediction*, San Antonio, TX, Amer. Meteor. Soc., 280-283.

Fox-Rabinovitz, M.S., G.L. Stenchikov, M.J. Suarez, L.L. Takacs, and R.C. Govindaraju, 2000: A uniform- and variable-resolution stretched-grid GCM dynamical core with realistic orography. *Mon. Wea. Rev.*, **128**, 1883-1898.

Freitas, S.R., K.M. Longo, M.A.F. Silva Dias, R. Chatfield, P. Silva Dias, P. Artaxo, M.O. Andreae, G. Grell, L.F. Rodriguez, A. Fazenda, and J. Panetta, 2009: The coupled aerosol and tracer transport model to the Brazilian developments on the Regional Atmospheric Modeling System (CATT-BRAMS)-Part I: Model description and evaluation. *Atmos. Chem. Phys*., **9**, 2843-2861.

Gerard, L., J.-M. Piriou, R. Brozkova, J.-F. Geleyn, and D. Banciu, 2009: Cloud and precipitation parameterization in a meso-gamma-scale operational weather prediction model. *Mon. Wea. Rev.*, **137**, 3960-3977.

Gomes, J.L., and S.C. Chou, 2010: Dependence of partitioning of model implicit and explicit precipitation on horizontal resolution. *Meteorol. Atmos. Phys*., **106**, 1-8.

Grell., G.A., 1993: Prognostic evaluation of assumptions used by cumulus parameterizations. *Mon. Wea. Rev.,* **121**, 764-787.

Grell., G.A., and D. Devenyi, 2002: A generalized approach to parameterizing convection combing ensemble and data assimilation techniques. *Geophys. Res. Let.,* **29**, NO. 14, 1693, 10.1029/2002GL015311.

Grell, G.A, and S. R. Freitas, 2014: A scale and aerosol aware stochastic convective parameterization for weather and air quality modeling. *Atmos. Chem. Phys.,* **14**, 5233-5250.

Guichard, F., J.C. Petch, J.-L. Redelsperger, P. Bechtold, J.-P. Chaboureau, S. Cheinet, W. Grabowski, H. Grenier, C.G. Jones, M. Köhler, J.-M. Piriou, R. Tailleux, and M. Tomasini, 2004: Modelling the diurnal cycle of deep convection over land with cloud-resolving models and single-column models. *Quart. J. Roy. Meteor. Soc*., **130**, 3139-3172.

Hong, S.-Y., and J.-O. Lim, 2006: The WRF single-moment 6-class microphysics scheme (WSM6). *J. Korean Meteor. Soc*., **42**, 129-151.

Huffman, G.J., R.F. Adler, D.T. Bolvin, and E.J. Nelkin, 2010: The TRMM Multi-Satellite Precipitation Analysis (TMPA). Chapter 1 in Satellite Rainfall Applications for Surface Hydrology, F. Hossain and M. Gebremichael, *Eds. Springer Verlag,* ISBN: 978-90-481-2914-0, 3-22.

Iacono, M.J., E.J. Mlawer, S.A. Clough, and J.-J. Morcrette, 2000: Impact of an improved longwave radiation model, RRTM, on the energy budget and thermodynamic properties of the NCAR Community Climate Model, CCM3. *J. Geophys. Res*., **105**, NO. D11, 14873-14890.

Ju, L., T. Ringler, and M. Gunzburger, 2011: Voronoi tessellations and their applications to climate and global modeling. *Numerical Techniques for Global Atmospheric Models.,* P. Lauritzen et al., Eds., Springer, 313-342.

Jung, J.-H., and A. Arakawa, 2004: The resolution dependence of model physics: Illustrations from nonhydrostatic model experiments. *J. Atmos. Sci.,* **61**, 88-102.

Kain, J.S., 2004: The Kain-Fritsch convective parameterization: An update. *J. Appl. Meteorol*., **43**, 170-181.

Kain, J.S., and J.M. Fritsch, 1993: Convective parameterization for mesoscale models: The Kain-Fritsch scheme. *The Representation of Cumulus Convection in Numerical Models, Meteor. Monogr,* No. 24, Amer. Meteor. Soc., 165-170.

Klemp. J.B., 2011: A terrain-following coordinate with smoothed coordinate surfaces. *Mon. Wea. Rev*., **139**, 2163-2169.

Klemp, J.B., W.C. Skamarock, and J. Dudhia, 2007: Conservative split-explicit time integration methods for the compressible nonhydrostatic equations. *Mon. Wea. Rev*., **135**, 2897-2913.

Kuell, V., A. Gassmann, and A. Bott, 2007: Towards a new hybrid cumulus parameterization scheme for use in non-hydrostatic weather prediction models. *Quart. J. Roy. Meteor. Soc.,* **133**, 479-490.

Mesinger, F., Z.I. Janjic, S. Nickovic, D. Gavrilov, and D.G. Deaven, 1988: The step-mountain coordinate: Model description and performance for cases of alpine lee cyclogenesis and for a case of an appalachian redevelopment. *Mon. Wea. Rev*., **116**, 1493-1518.

Mlawer, E.J., S.J. Taubman, P.D. Brown, M.J. Iacono, and S.A. Clough, 1997: RRTM, a validated correlate-k model for the longwave. *J. Geophys. Res*., **102**, NO. D14, 16663-16682.

Nakanishi, M., and H. Niino, 2009: Development of an improved turbulence closure model for the atmospheric boundary layer. *J. Meteor. Soc. Japan*, **87**, 895-912.

Park, S.-H., W. C. Skamarock, J.B. Klemp, L.D. Fowler, and M.G. Duda, 2013: Evaluation of global atmospheric solvers using extensions of the Jablonowski and Williamson baroclinic wave test case. *Mon. Wea. Rev*., **141**, 3116-3129.

Ringler, T.D., L.D. Ju, and M. Gunzburger, 2008: A multiresolution method for climate system modeling: applications of spherical Voronoi tessellations. *Ocean Dyn.,* **58**, 475-498.

Ringler, T.D., J. Thuburn, J.B. Klemp, and W.C. Skamarock, 2010: A unified approach to energy conservation and potential vorticity dynamics for arbitrarily-structured C-grids. *J. Comput. Physics*, **229**, 3065-3090.

Satoh, M., T. Masuno, H. Tomita, H. Miura, T. Nasuno, and S. Iga, 2008: Nonhydrostatic icosahedral atmospheric model (NICAM) for global cloud resolving model simulations. *J. Comput. Phys.*, **227**, 3486-3514.

Satoh, M., T. Inoue, and H. Miura, 2010: Evaluations of cloud properties of global and local cloud system resolving models using CALIPSO and CloudSat simulators. *J. Geophys. Res.,* **115**, D00H14, doi:10.1029/2009JD012247.

Simpson, J., R.H. Simpson, D.A. Andrews, and M.A. Eaton, 1965: Experimental cumulus dynamics. *Rev. Geophys*., **3**, 387-431.

Simpson, J., and V. Wiggert, 1969: Models of precipitating cumulus towers. *Mon. Wea. Rev*., **97**, 471-489.

Skamarock, W.C., and A. Gassmann, 2011: Conservative transport schemes for spherical geodesic grids: High-order flux operators for ODE-based time integration. *Mon. Wea. Rev*., **139**, 2962-2975.

Skamarock, W.C., J.B. Klemp, M.G. Duda, L.D. Fowler, S.-H. Park, and T.D. Ringler, 2012: A multiscale nonhydrostatic atmospheric model using Centroidal Voronoi tessellations and C-grid staggering. *Mon. Wea. Rev*., **140**, 3090-3105.

Skamarock, W.C., J.B. Klemp, J. Dudhia, D.O. Gill, D.M. Barker, M. G. Duda, X.-Y. Huang, W. Wang, and J.G. Powers, 2008: A description of the Advanced Research WRF Version 3. NCAR technical note, National Center for Atmospheric Research, Boulder, Colorado, USA, available at http://www.mmm.ucar.edu/wrf/users/docs/arw_v3.pdf (7 May 2014).

Smagorinsky, J., 1963: General circulation experiments with the primitive equations. I. The basic experiment. *Mon. Wea. Rev*., **91**, 99-164.

Takayabu, Y.N., 2002: Spectral representation of rain profiles and diurnal variations observed with TRMM PR over the equatorial area. *Geophys. Res. Let.,* **29**, NO. 12, 1584, 10.1029/2001GL014113.

Tiedtke, M., 1989: A comprehensive mass flux scheme for cumulus parameterization in large-scale models. *Mon Wea. Rev*., **117**, 1779-1800.

Walko, R.L., and R. Avissar, 2008: The Ocean-Land-Atmosphere Model (OLAM). Part I: Shallow-water tests. *Mon. Wea. Rev*., **136**, 4033-4044.

Wicker, L.J., and W.C. Skamarock, 2002: Time-splitting methods for elastic models using forward time schemes*. Mon. Wea. Rev*., **130**, 2088-2097.

Wu, C.-M., and A. Arakawa, 2014: A unified representation of deep moist convection in numerical modeling of the atmosphere. Part II. *J. Atmos. Sci.,* 2089-2013.

Xu, K.-M., and D.A. Randall, 1996: A semiempirical cloudiness parameterization for use in climate models. *J. Atmos. Sci*., **53**, 3084-3102.

Yeh, K.-S., J. Cote, S. Gravel, A. Methot, A. Patoine, M. Roch, and A. Staniforth, 2002: The CMC-MRB Global Environmental Multiscale (GEM) model. Part III: Nonhydrostatic formulation. *Mon. Wea. Rev*., **130**, 339-356.

TABLE 1: Horizontal mesh resolutions, minimum and maximum distance between grid-cell centers, time-steps, horizontal diffusion length scales, and convective cloud fraction for experiments with the quasi-uniform and variable-resolution meshes.

	QU50	NS50	QU15	NS15	GF70	GFNS	NOGF
No. Cells	256,002	256,002	2,621,442	2,621,442	6,848,514	6,848,514	6,848,514
Min. Cell distance (km)	37.3	37.3	11.0	11.0	2.2	2.2	2.2
Max. Cell distance (km)	50.9	50.9	15.9	15.9	60.2	60.2	60.2
Time-step (s)	360	360	90	90	12	12	12
Diffusion length scale (km)	50	50	15	15	3	3	3
$(1-\sigma)^2$	0.980	1	0.785	1	Fig. 1.c	1	Fig. 1.c

TABLE 2: 50°N-50°S spatially averaged precipitation rates for the different experiments, TMPA data, and the GFS forecast. Units are mm day^{-1}.

	QU50	NS50	QU15	NS15	TMPA	KF50	KF15	TD50	TD15	GFS
PRECIP. (mm day^{-1})	2.92	2.92	2.86	2.91	3.13	3.02	2.87	3.59	2.94	2.73

TABLE 3: Global mean convective, grid-scale, and total precipitation rates for the different experiments with the GF, TD, and KF convective parameterizations. Units are mm day^{-1}.

	QU50	NS50	QU15	NS15	TD50	TD15	KF50	KF15
CONVECTIVE (mm day^{-1})	2.09	2.10	1.88	2.05	1.98	1.46	2.26	1.98
GRID-SCALE (mm day^{-1})	1.35	1.34	1.49	1.37	1.60	1.98	1.27	1.38
TOTAL (mm day^{-1})	3.44	3.44	3.37	3.42	3.58	3.44	3.53	3.36

LIST OF TABLES

LIST OF FIGURES

Figure 12: Vertical distribution of the a) cloud water mixing ratio (g kg^{-1}); b) cloud ice mixing ratio (g kg^{-1}), and c) grid-scale horizontal cloud fraction (%) simulated with GF70 (black line), GFNS (red line), and NOGF (blue line).

Figure 13: Temperature difference (left panels) and zonal wind difference (right panels) between GF70 and GFNS over the area of mesh refinement at 200 hPa (top panels), 500 hPa (middle panels), 850 hPa (bottom panels). Units are K for temperature and m s^{-1} for zonal wind.

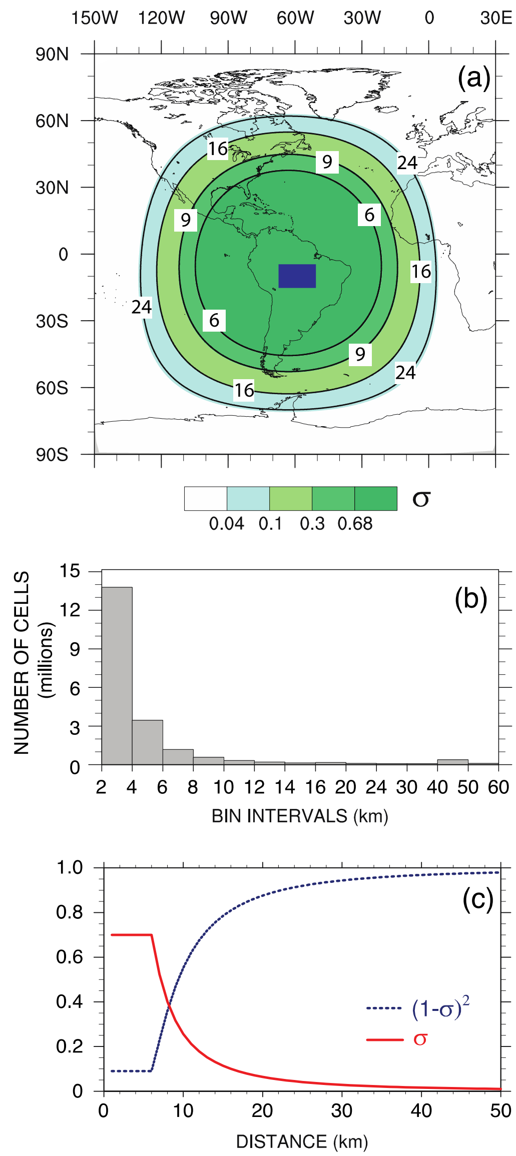

Figure 1: a) Refined area of the variable-resolution mesh over South America depicted using isolines of the mean distance between grid-cell centers (km) and filled contours of the convective cloud fraction (dimensionless); b) histogram of the number of grid cells as a function of the mean distance between grid-cell centers; and c) convective updraft fraction as a function of the mean distance between grid-cell centers.

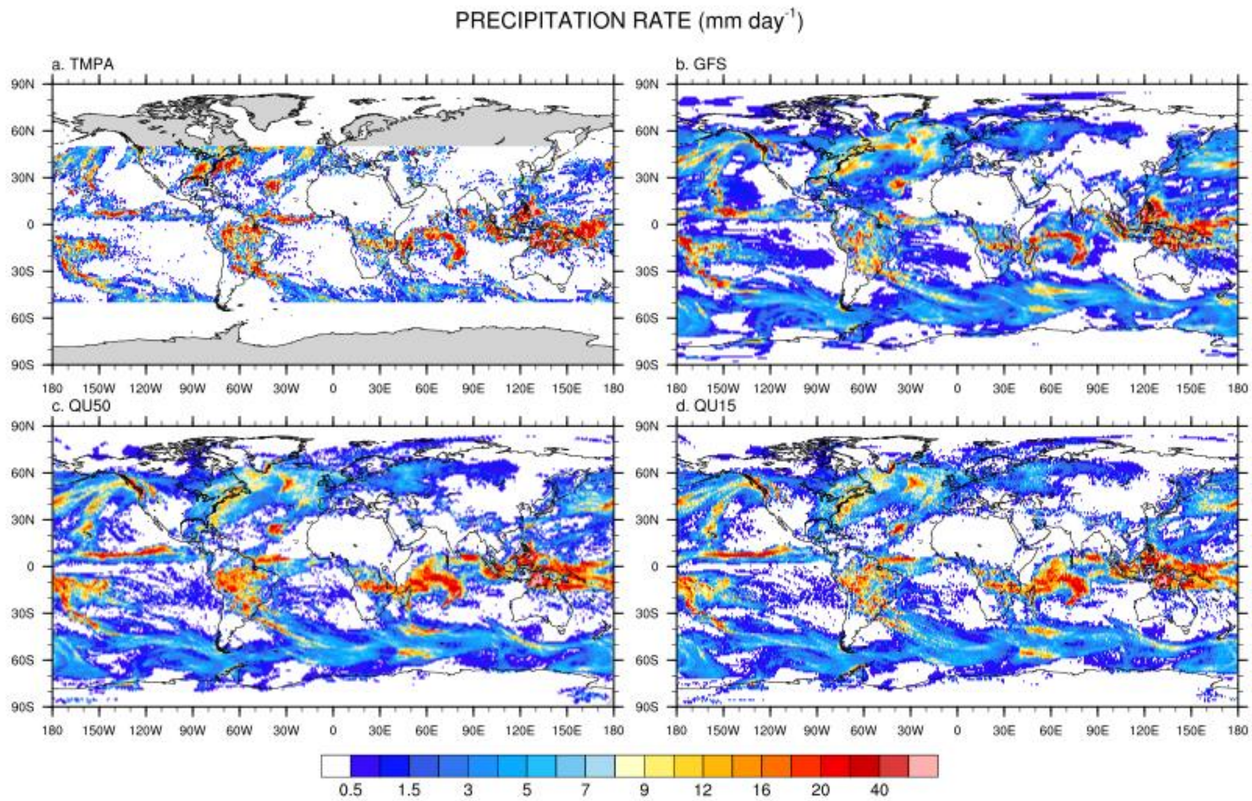

Figure 2: Geographical distribution of the precipitation rate calculated between 0000 UTC 11 January 2014 and 0000 UTC 14 January 2014 obtained from a) TMPA satellite data and b) GFS forecast; and simulated with c) QU50 and d) QU15. Units are mm day^{-1}.

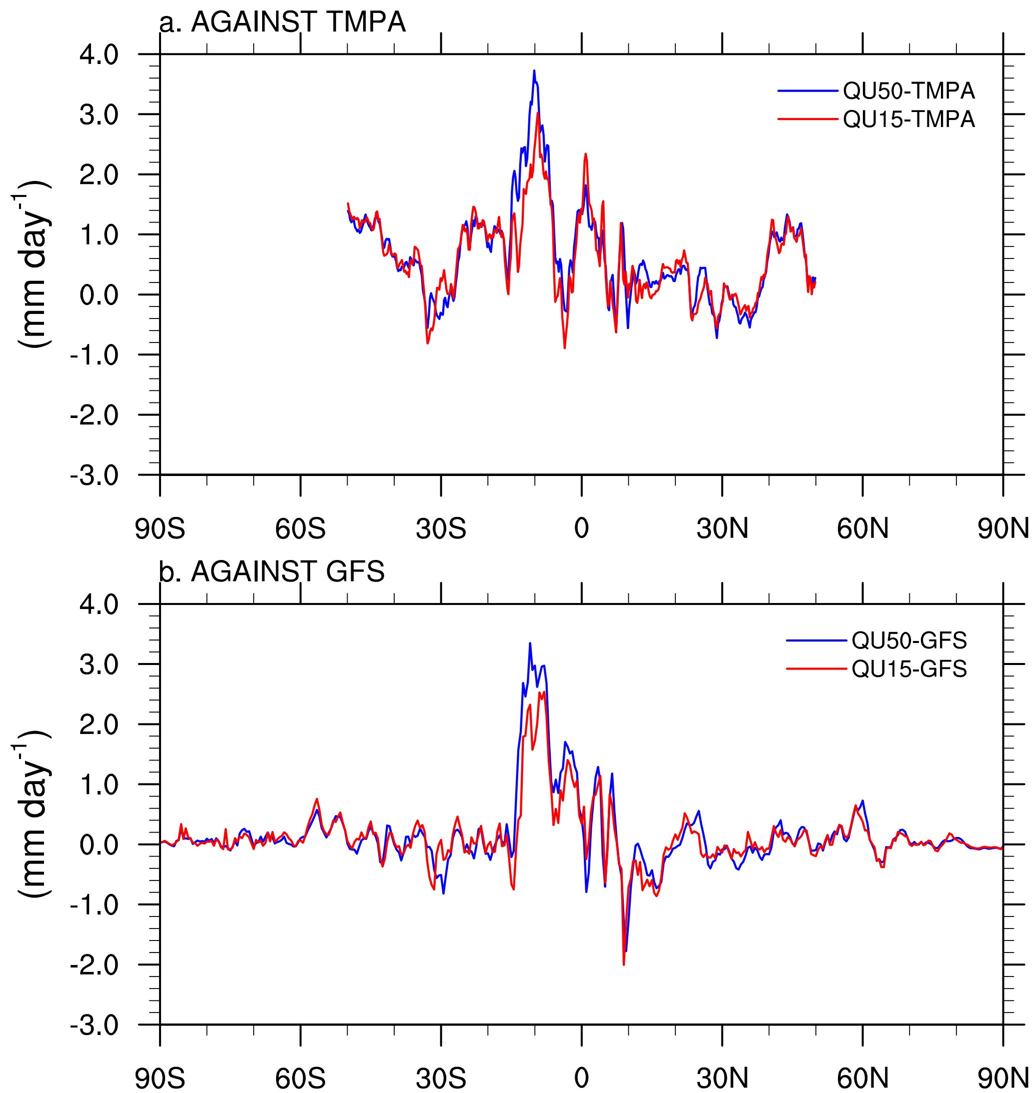

Figure 3: Zonal mean differences in the precipitation rate calculated between 0000 UTC 11 January 2014 and 0000 UTC 14 January 2014 between a) QU50, QU15 and TMPA data; and b) QU50, QU15, and GFS forecast. Units are mm day^{-1}.

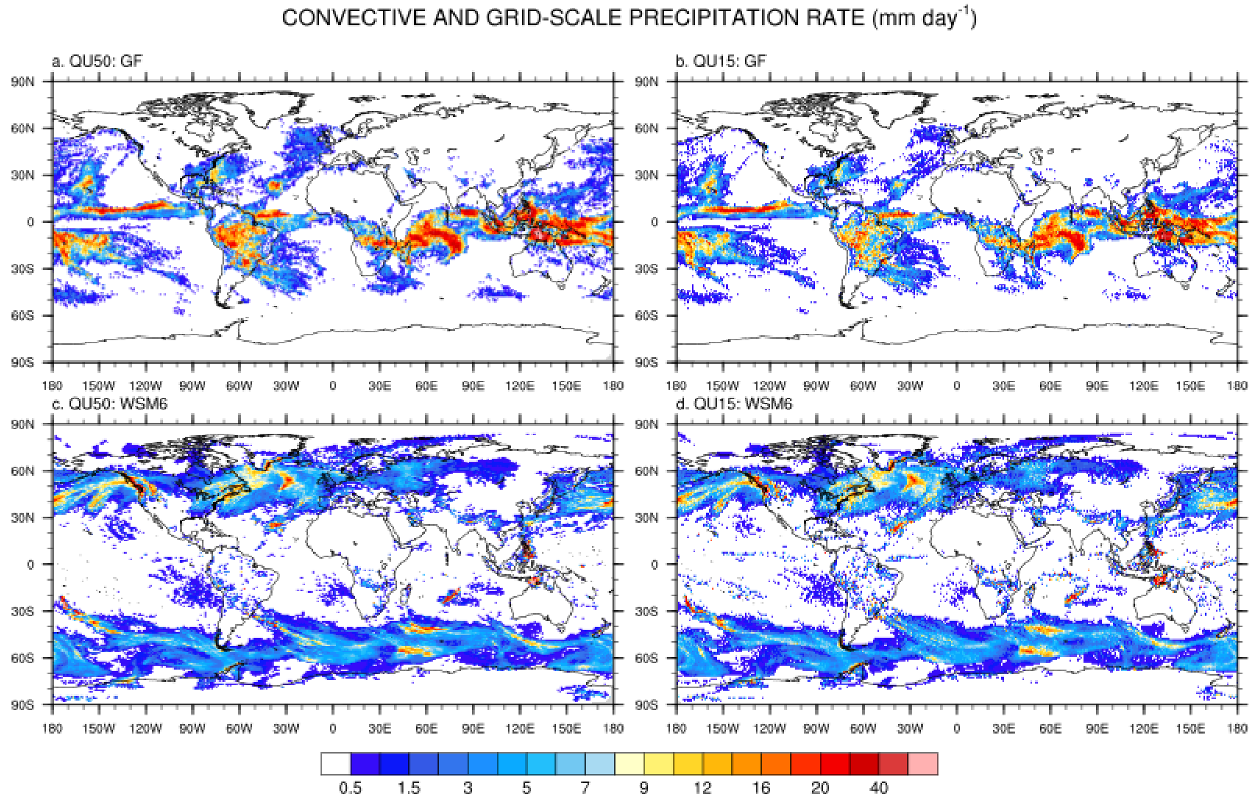

Figure 4: Geographical distribution of the convective precipitation rate calculated between 0000 UTC 11 January 2014 and 0000 UTC 14 January 2014 and simulated with a) QU50 and b) QU15; and the grid-scale precipitation rate calculated between 0000 UTC 11 January 2014 and 0000 UTC 14 January 2014 and simulated with c) QU50 and d) QU15. Units are mm day^{-1}.

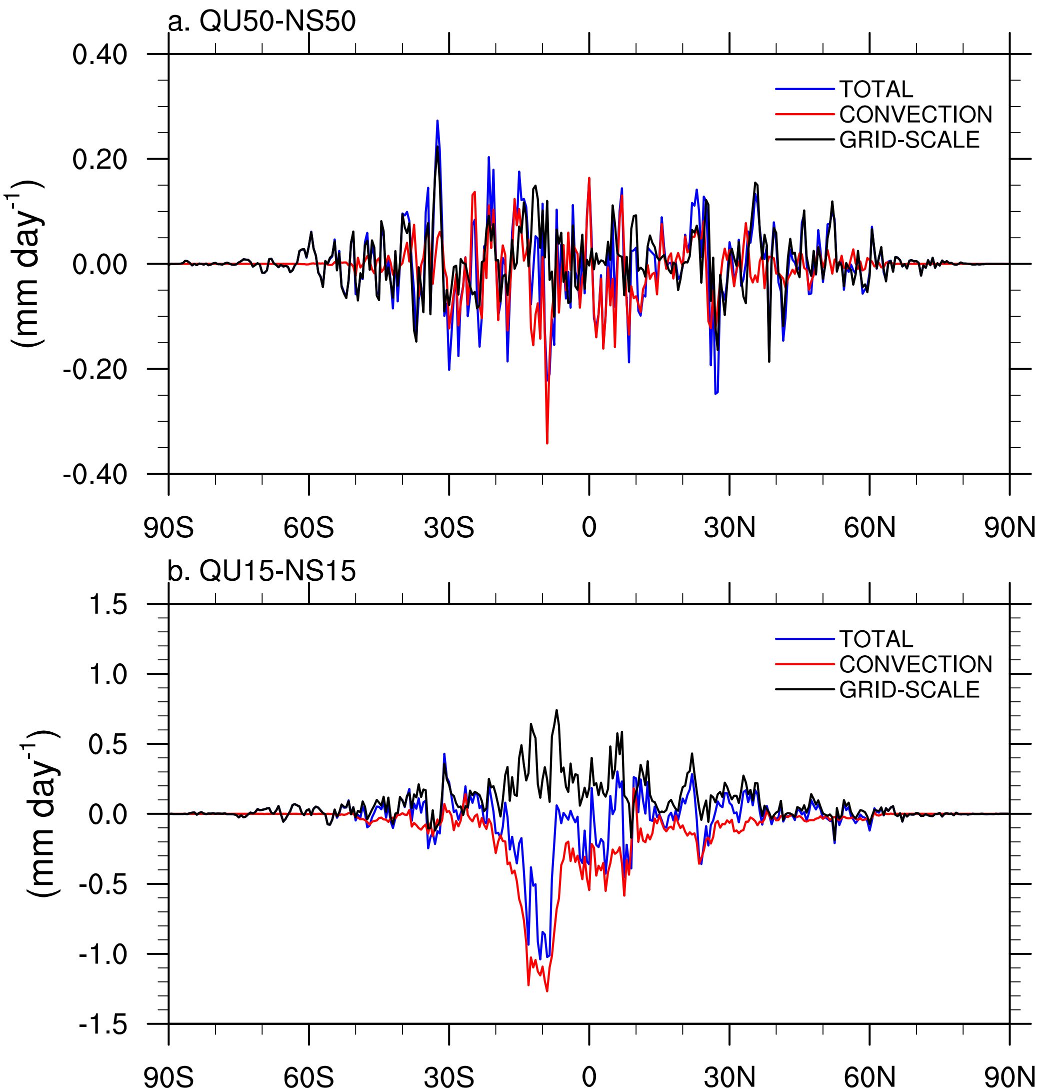

Figure 5: Zonal mean differences in total, convective, and grid-scale precipitation rates calculated between 0000 UTC 11 January 2014 and 0000 UTC 14 January 2014: a) QU50 minus NS50; and b) QU15 minus NS15. Units are mm day^{-1}.

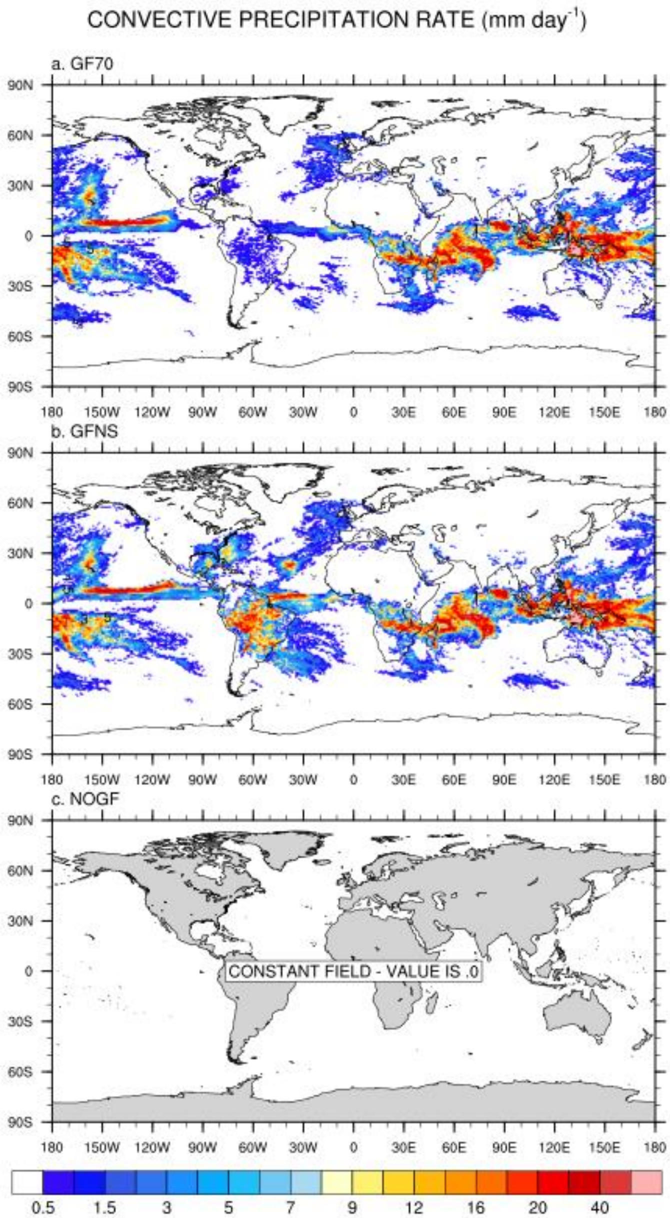

Figure 6: Geographical distribution of the convective precipitation rate calculated between 0000 UTC 11 January 2014 and 0000 UTC 14 January 2014 and simulated with a) GF70; b) GFNS; and c) NOGF. Units are mm day^{-1}.

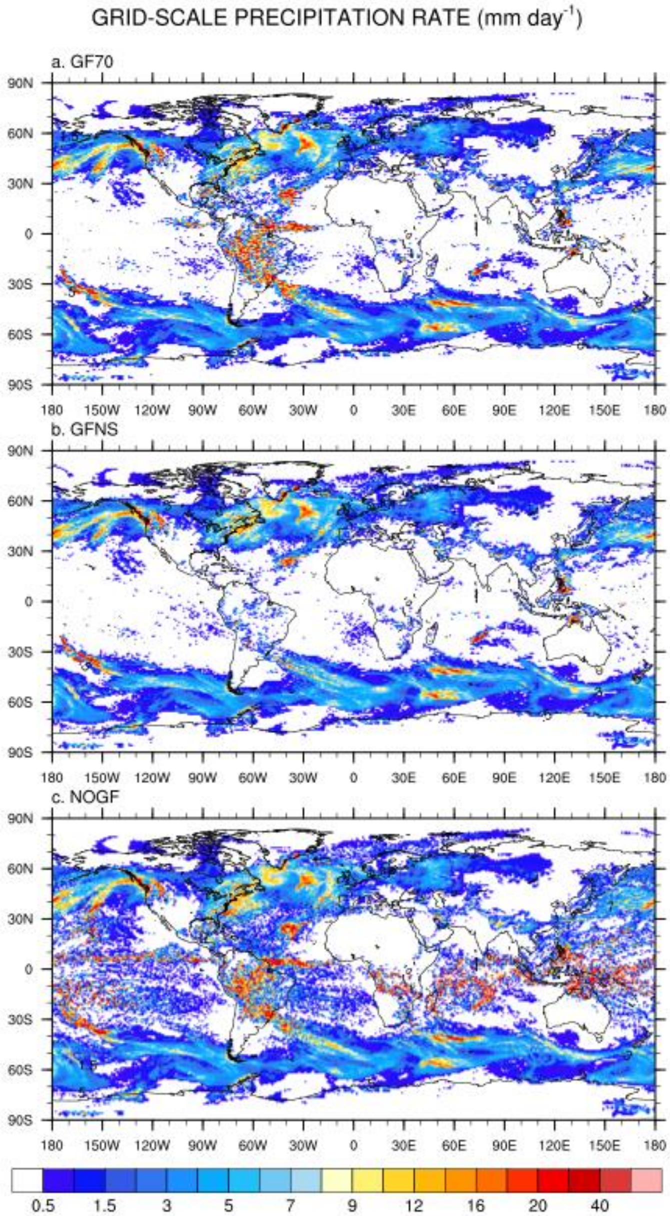

Figure 7: As Fig. 6, but for the grid-scale precipitation rate.

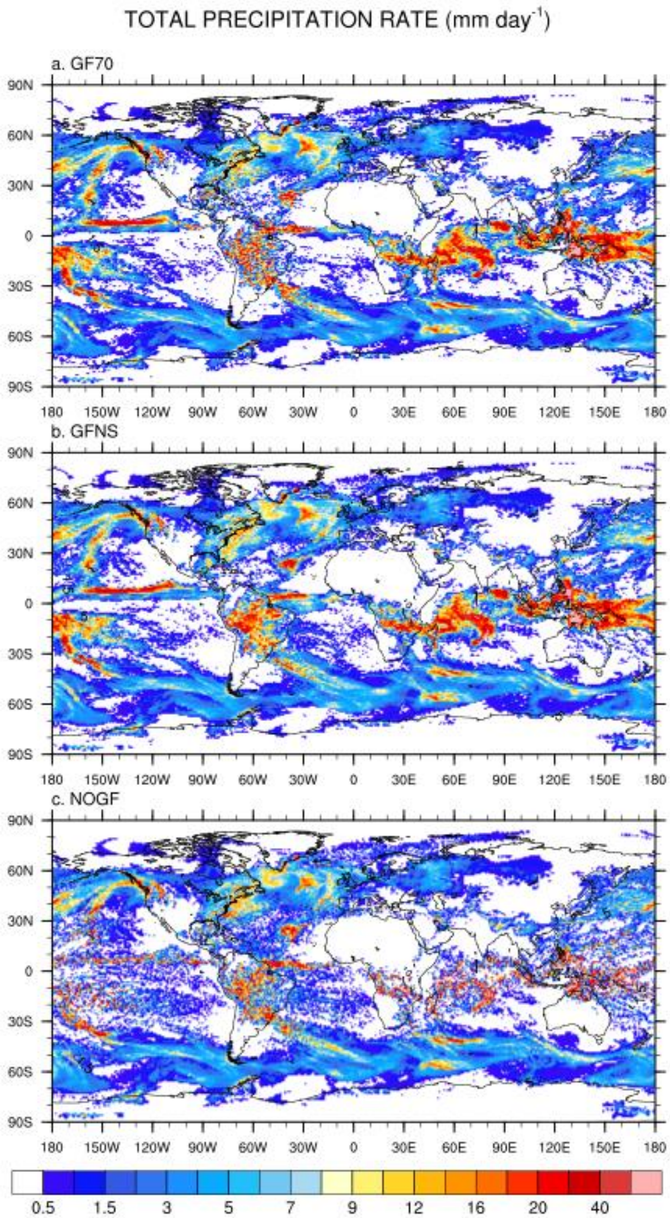

Figure 8: As Fig. 6, but for the total precipitation rate.

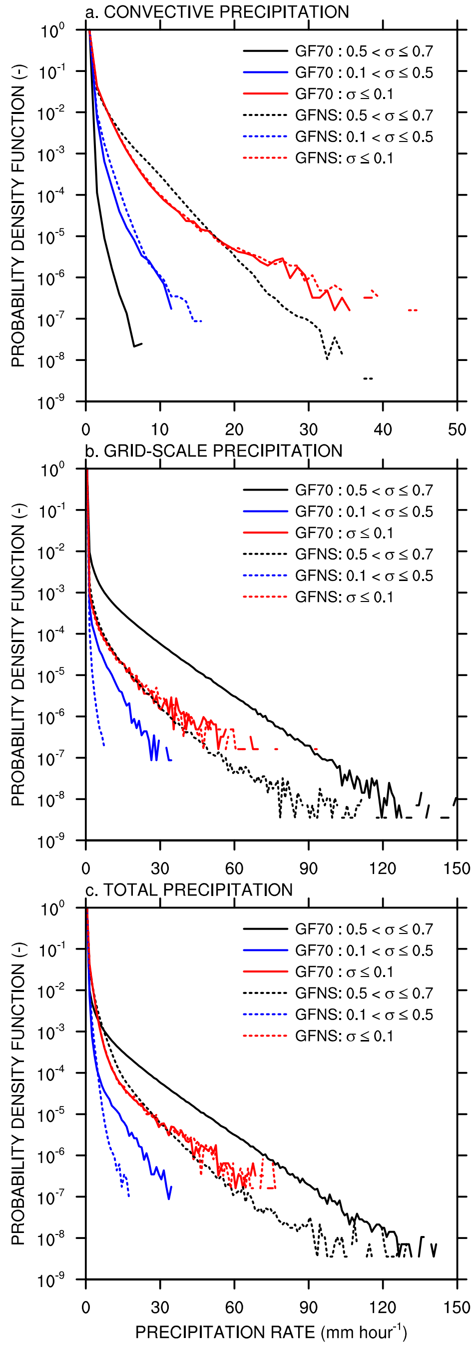

Figure 9: Probability density distributions of the a) convective precipitation rate; b) grid-scale precipitation rate; and c) total precipitation rate for GF70 (solid lines) and GFNS (dashed lines) as functions of the convective updraft fraction. Units are mm hour^{-1}.

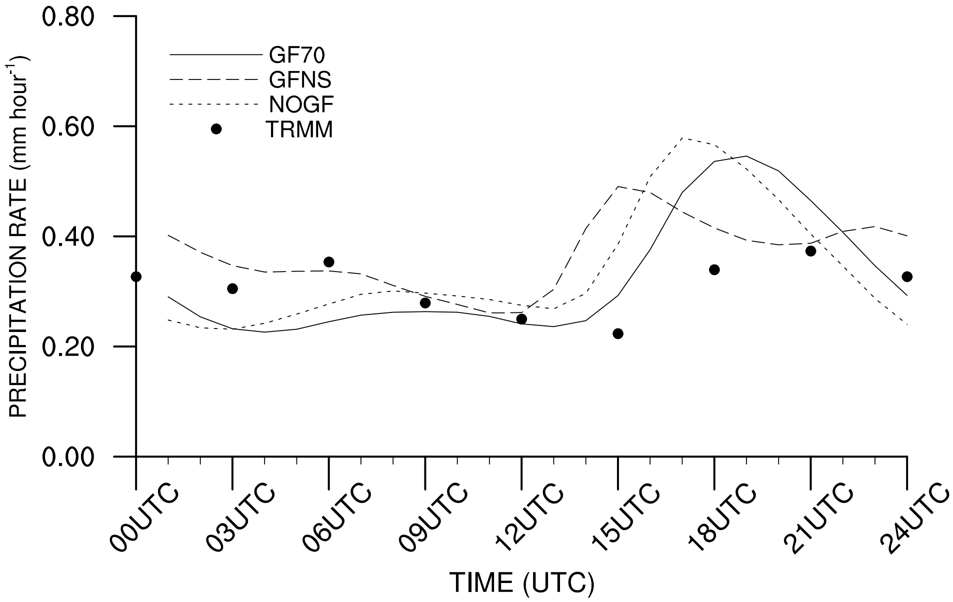

Figure 10: Diurnal cycle of the precipitation rate simulated with GF70 (solid line), GFNS (dashed line), NOGF (dotted line), and TMPA data (dots). Units are mm hour^{-1}.

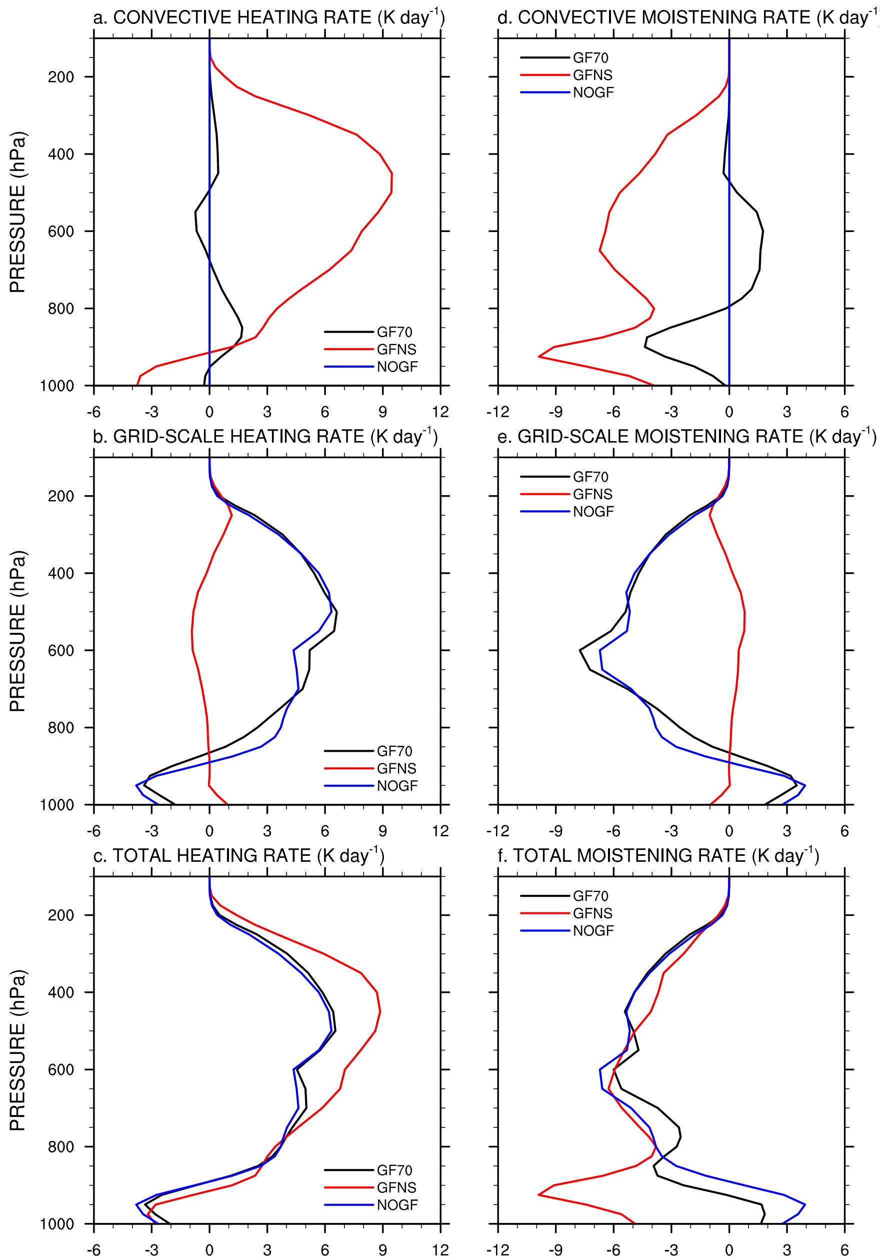

Figure 11: Vertical distribution of a) the convective heating rate, b) the grid-scale heating rate, and c) the convective plus grid-scale heating rate simulated with GF70 (black line), GFNS (red line), and NOGF (blue line). Units are K day^{-1}.

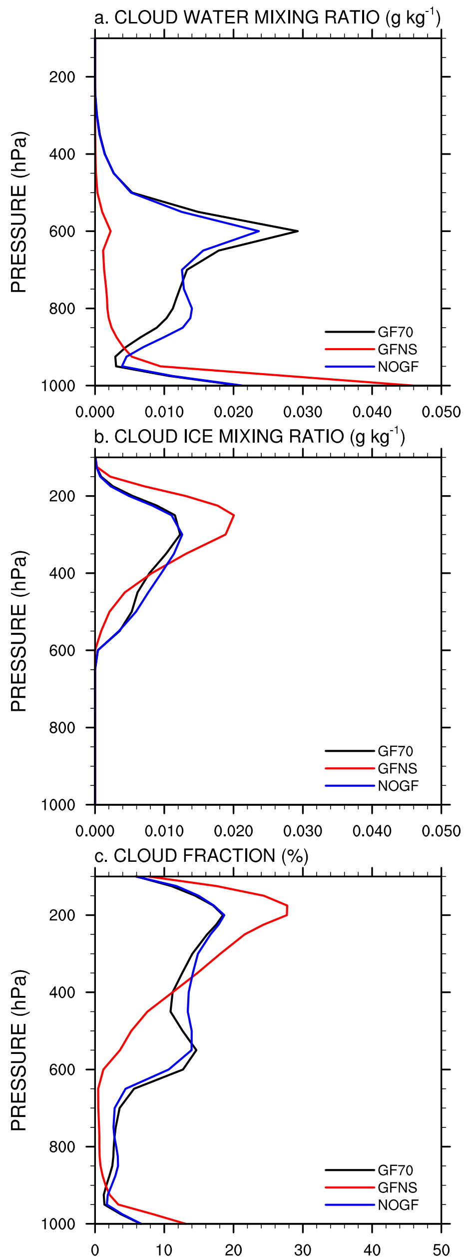

Figure 12: Vertical distribution of the a) cloud water mixing ratio (g kg^{-1}); b) cloud ice mixing ratio (g kg^{-1}), and c) grid-scale horizontal cloud fraction (%) simulated with GF70 (black line), GFNS (red line), and NOGF (blue line).

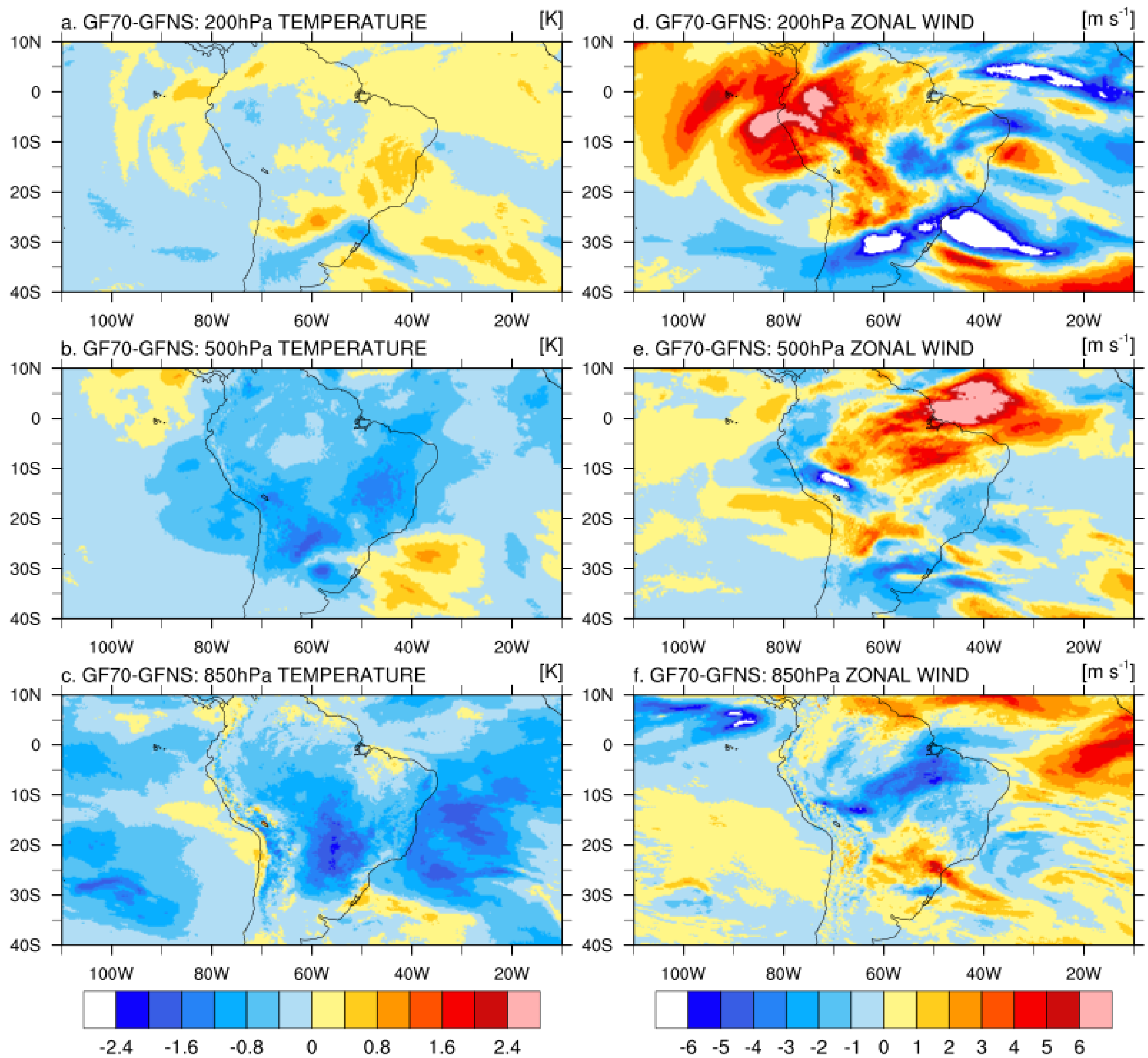

Figure 13: Temperature difference (left panels) and zonal wind difference (right panels) between GF70 and GFNS over the area of mesh refinement at 200 hPa (top panels), 500 hPa (middle panels), 850 hPa (bottom panels). Units are K for temperature and m s^{-1} for zonal wind.